EPJ Web of Conferences **344**, 01012 (2025) https://doi.org/10.1051/epjconf/202534401012
AIPTEC 2025

Enhancing the efficiency of a gravitational water vortex turbine through blade length and exit angle optimization

Lailatus Sa'diyah Yuniar Arifianti[1*], *Mohammad* Rizanto Juliarsyah[2], *Irwanda*. Y.P.[2], *Khoirul.* A.[2], *Sudirman* Rizki Ariyanto[1], *Ferly* Isnomo Abdi[1], *Fithrotul* Irda Amaliah[3], *Yustin* Setiya Widoretno[1], *Himmawan* S.M.[4]

[1]Department of Automotive Engineering Technology, Universitas Negeri Surabaya, Ketintang, Surabaya, 60231, Indonesia
[2]Department of Mechanical Engineering, Malang State Polytechnic, Jl. Soekarno Hatta No.9, Malang,65141 Indonesia
[3]Departement of Electrical Engineering, Universitas Negeri Surabaya, Ketintang, Surabaya, 60231, Indonesia
[4]Departement of Mechanical and Energy, Politeknik Elektronika Negeri Surabaya, Jl. Raya ITS Sukolilo Surabaya 6011, Indonesia

Abstract. GWVTs make possible micro-hydropower at ultra-low heads where conventional turbines are impractical. This study targets the persistent gap of suboptimal runner design and outlet losses through the optimization of a radial closed-hub GWVT for reliable high-efficiency operation under low head. The contribution of this research is a compact, reproducible CFD-Taguchi L9 workflow ranking runner parameters by importance, linking vortex descriptors to performance; the research contribution is an engineering design map (N, L, β_1, β_2) that can be directly applied at low-head sites. Methods include the use of free-surface CFD (VOF, steady RANS k–ε, MRF) together with a mesh-independence study and a Taguchi L9 array to span the number of blades, N, blade length, L, entry angle, β_1, and exit angle, β_2. Simulations were run at $Q \approx 0.6$ m³/s and $H \approx 0.86$ m; torque/efficiency and flow fields (λ_2 iso-surfaces, VOF α=0.5) were analyzed. Results indicate torque plateaus from ≥0.8 million cells; a ≈2.22-million-cell grid offers a sound accuracy-cost trade-off. The main-effects ranking is $L > \beta_2 > N \approx \beta_1$. The optimum (N=13, L=45°, β_1=11.51°, β_2=3°) provides 628 N·m and ≈58.8% efficiency (≈+89% torque vs. baseline), along with a deeper, more axisymmetric core with cleaner discharge. This implies that the most effective levers for performance are lengthening the blades and minimizing the exit angle. This workflow now provides a practical path to robust design. Confirmation runs, URANS/LES, and prototype testing will follow in due course, and generalization to field conditions will be carried out.

1 Introduction

Micro-hydropower is an efficient way of extending access to low-carbon, low-cost electricity at ultra-low heads where Kaplan, Francis, or Pelton turbines are either not economic or not possible [1–3]. Among new concepts, the gravitational water vortex turbine (GWVT) exploits a rotating free-surface vortex in a short basin to extract energy at heads below about one meter with comparatively small civil works and very good site flexibility [1,4–7]. Inflow—tends to be tangential, sloping, or spiral—gives rise to circulation; a vortex of air is created and redistributes shear and pressure near the core, enabling a runner to harness torque from swirl and pressure drop [5–8].

The free-surface vortex physics enhances GWVT performance: conservation of angular momentum enhances circumferential velocity towards the core, with air entrainment and free-surface deformation controlling pressure gradients and dissipation channels directly impacting efficiency [6–7,14]. Vortex height, core diameter, and circulation prediction generally employ volume-of-fluid (VOF) multiphase CFD with RANS closures (e.g.,–ε, k–ω) cross-validated with laboratory measurement and fine vortex-profile characterization [6–7,11,14,23]. Analytical models of strong free-surface vortices provide first-cut scaling and bounds before higher-fidelity CFD resolution and experimentation [14].

Coupled geometry leads to device-level performance. The inlet (inclination/spiral) controls swirl strength and inflow uniformity; basin shape (conical vs cylindrical) influences vortex stability; the discharge cone damps outflow to reduce negative pressure gradients; and runner parameters—number of blades, length/twist/angles, diameter ratios, and axial position—dictate coupling to swirling boundary layer and air core [2–7,9,12]. Recent research emphasizes runner position/constraint constraints and their interrelation with conical basins and spiral or inclined intakes [20], and experimental trends of rotor performance at low heads [21]. Generally, conical basins with spiral or inclined intakes and runners optimally placed lead to stronger and more stable vortices and more efficient operation under the same head and discharge [2,4–7,9,12,20–21].

Methodologically, design-of-experiments (DoE) and response-surface/surrogate modeling enable efficient exploration of multi-parameter domains and near-optimum configuration identification at fewer costly

* Corresponding author: lailatusarifianti@unesa.ac.id

evaluations. Latest reports demonstrate confirmed gains through RSM-assisted optimization of runner shape and position, and—in recent times—simultaneous optimization of inlet channel, spiral basin, and discharge cone coupled with the runner [3–5,8–9]. CFD–experimental co-verification reinforces the predictive confidence of efficiency and flow descriptors even more, closing the simulation-prototyping loop [11,24].

Some remaining gaps notwithstanding, most studies still optimize subsystems independently and not co-optimize inlet–basin–discharge–runner variables under shared hydraulic constraints, maybe resulting in suboptimal global performance [1,4–6,9,25]. Cross-study comparison is challenged by different meshing, boundary conditions, and turbulence models; systematic verification and validation would need to establish correlation of vortex metrics (core size, circulation, free-surface profile) with confidence to efficiency [1,6–7,11,14,23,24]. Sustainability and manufacturability—e.g., with natural-fiber composite and additive manufacturing—are underreported; prototyping and testing pipelines have promising pathways but require more ubiquitous benchmarking against metallic rotors under hydrodynamic loading and abrasion [10,22]. Techno-economic assessment for rural microgrids and infrastructure retrofits is ultimately challenging due to field-scale datasets over seasonal variability remaining scarce [8,17,25].

This research addresses these requirements through an integrated optimization of a vortex water turbine for micro-hydropower. We design inlet geometry, basin conicity, discharge cone, and runner parameters on paradigm ultra-low-head regimes, and we couple free-surface CFD (VOF with highly robust turbulence closure) to statistically optimal DoE/response-surface analysis, followed by validation and benchmarking against best-available settings under matched head and flow [2–5,8–9,11–12,20–21,24–25]. The research contribution is: (i) a coherent, physics-constrained multi-parameter optimization strategy that optimizes inlet–basin–discharge–runner parameters simultaneously; (ii) experiment-confirmed CFD–DoE–RSM process linking measurable vortex descriptors to turbine efficiency; (iii) test-guided geometry–location map for runner and conical basins with spiral or inclined inlets; (iv) engineering design considerations for materials and manufacturability; and (v) transparent methodological flow and literature-synched benchmarking procedure to facilitate replication.

2 Research method

2.1 Literature review

The development of micro-hydropower technologies is gaining increasing importance in efforts to improve access to renewable energy, particularly in rural and remote areas. Among all the technologies contemplated, the Gravitational Water Vortex Turbine (GWVT) offers a viable solution to low-head (< 3 m) cases where traditional turbines such as Pelton, Francis, or Kaplan are economically or technically impractical. The GWVT principle utilizes the rotational energy of vortex flow induced in a spiral or cylindrical basin, where the vortex core can be accessed by a vertically mounted runner on a shaft. According to [26, 27], the main advantage of the GWVT is design simplicity, absence of guide vanes, and the capability to perform well at extremely low heads and discharges. The core of hydropower analysis is the elementary equation for hydraulic power output, and it is characterized as:

$$Ph = \rho \; x \; g \; x \; Q \; x \; H \tag{1}$$

Where:
P_h = Hydraulic Power (watts)
ρ = density of water (kg/m³), typically 1000
g = gravitational acceleration (9.81 m/s²)
Q = flow rate (m³/s)
H = available head (m).

This equation defines the theoretical power that can be harnessed from a given water source. However, the actual mechanical power obtained from the turbine is less than this due to various losses. The efficiency of the turbine η_t is thus defined as:

$$\eta t = \frac{P_{out}}{P_h} = \frac{T \; x \; \omega}{\rho \; x \; g \; x \; Q \; x \; H} \tag{2}$$

Where:
P_{out} = actual mechanical power output (W)
T = torque generated at the shaft (Nm)
ω = angular velocity of the runner (rad/s).

A number of investigations have been aimed at optimizing the hydraulic efficiency of GWVTs by improving various components such as intake basin shape, runner geometry, and flow conditioning. [28] made a comparison between convex and concave conical basins and concluded that vortex core stability and flow uniformity are extremely important for performance. [29] emphasized maintaining tangential flow and damping asymmetric disturbances within the basin. In runner design, which directly affects torque and rotational efficiency, several parameters are thoroughly investigated:

- Number of blades (more blades can provide smoother torque, but also generate resistance)
- Blade length (which establishes the effective radius and moment arm)
- Inlet and outlet blade angles, which control how fluid enters and exits the blade passages.

Runner performance is commonly analyzed by Euler's turbine equation, which relates energy transfer to tangential components of velocity change:

$$g \; x \; H = U1 \cdot Vu1 - U2 \cdot Vu2 \tag{3}$$

Where:
U_1, U_2 = peripheral velocity of the runner at the inlet and outlet
V_{u1}, V_{u2} = tangential components of the absolute velocity at the inlet and outlet.

In a radial-flow GWVT, the incident flow has a considerable tangential component as a result of vortex rotation. Hence, runner blade geometry optimization is necessary to keep hydraulic losses to a minimum and to align blade entry angles with incident flow. Computational Fluid Dynamics (CFD) has become the de facto industry-standard tool for simulating and analyzing fluid flow in vortex turbines. As [30, 31] have shown, CFD has the ability to visualize flow fields, pressure contours, and vortex structures. It is particularly useful in GWVTs because it is hard to model the air–water interface (free surface) and vortices' behavior analytically. In the current research, the VOF (Volume of Fluid) technique is used for tracking the free surface, and the standard k-ε turbulence model is used to incorporate turbulent effects. CDM simulation is not sufficient to get optimum design parameters, especially when there are interactions between different variables. Hence, optimization techniques such as the Taguchi method are utilized. The Taguchi method, Design of Experiments (DOE) technique, utilizes orthogonal arrays for systematically varying the input parameters with a minimal number of simulations or experiments. The method applies a statistical measure known as the Signal-to-Noise (S/N) Ratio that is utilized for quantifying performance robustness. For optimization problems (e.g., efficiency maximization), the "larger-is-better" S/N ratio is calculated by:

$$S\,/\,N \;=\; -10 \times \log 10\ (\frac{1}{n}\sum_{i=1}^{n}\frac{1}{y_i^2} \qquad (4)$$

Where:
y_i = observed performance value (e.g., torque or efficiency)
n = number of repetitions or simulation runs.

[32, 33] applied the Taguchi method to investigate the impact of runner blade configuration and obtained a reduction in turbine torque of as much as 20%. The four parameters in this study that were selected for optimization are:

- Number of blades (N)
- Blade length (L)
- Inlet angle (β_1)
- Outlet angle (β_2)

All the parameters are experimentally tried in three levels, giving an L9 orthogonal array to optimize. This method enables the determination of the most critical factors and their optimal values with only nine simulation runs.

Finally, the work of [34] established that the incorporation of baffle plates within runner blades has been found to affect vortex shedding and reduce exit flow turbulence, but perhaps at the cost of increased design complexity. Hence, the combination of design, CFD simulation, and Taguchi optimization is a holistic method to improve vortex turbine performance in realistic microhydro-power operations.

Drawing on this literature foundation, this current work focuses on integrating design methods, simulation tools, and statistical optimization to produce a high-efficiency, low-cost, and scalable GWVT system suitable for rural Indonesia and other such environments' decentralized energy generation.

2.2 CFD simulation setup

Computational Fluid Dynamics (CFD) is essential for analyzing the flow characteristics, vortex development, and performance estimation of the Gravitational Water Vortex Turbine (GWVT) before physical modeling. In this research work, CFD simulations are utilized to study fluid behavior in the intake basin, runner, and tailrace under steady-state operating conditions. The simulation also allows for runner parameters to be optimized using a numerical procedure.

2.2.1 Software and solver settings

The simulations were carried out with ANSYS CFX software, which is finite volume-based commercial CFD software possessing strong multiphase flow capabilities and flexible meshing support. The governing equations employed in the simulation are the Navier-Stokes equations for incompressible, turbulent, multiphase flow. The chosen solver configuration is as follows:

- Type of Solver: Pressure-based solver, steady-state
- Type of Time Model: Steady (quasi-steady for rotating domains)
- Type of Multiphase Model: Volume of Fluid (VOF)
- Turbulence Model: Default k-ε (for general vortex prediction with high convergence stability)
- Gravity Direction: Negative Y-axis
- Rotation Frame: Transient Rotor-Stator (TRS) model for the runner zone

2.2.2 Mesh and domain

The simulation domain is divided into three parts: the tank, the runner, and the tailrace. The runner domain uses a rotating reference at 45 rpm, with the axis of rotation overlapping with the runner axis and the tank outlet. The types of meshes used in the three domains are different. The discharge channel uses a structured domain, the runner domain uses an unstructured mesh, and the tank domain uses a hybrid mesh, which is a combination of structured and unstructured meshes. Details of the solver settings and solver schemes used during the simulation can be seen in the next subsection. Figure 1 below shows the mesh and simulation domain previously worked on in a previous journal [35].

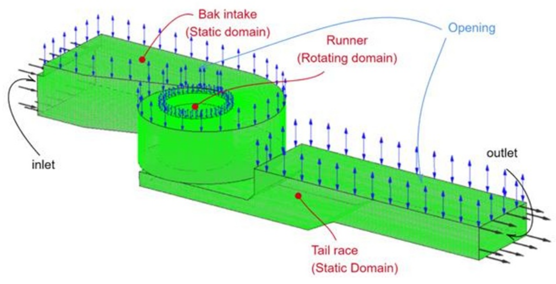

Fig. 1. Mesh and domain simulation.

Table 1. Mesh domain.

Domain	Node	Element	Mesh Type	Domain Type
Tub	145200	133572	Hibrida	Static
Runner	106706	550239	Unstructured	Rotating (45 rpm)
Tailrace	82622	75096	Structured	Static
Totally	334528	758907		

Fig. 1 depicts a physically faithful CFD arrangement where the tailrace/vortex basin and intake are fixed regions and the runner is a spinning region at 45 rpm; flow enters through the inlet, forms a free-surface vortex in the basin, interacts with the runner, and discharges through the opening/outlet. This meshing is in keeping with the mesh inventory: 334,528 nodes and 758,907 elements distributed as follows—basin: 145,200 nodes / 133,572 elements with a hybrid mesh suited to free-surface geometry; runner: 106,706 / 550,239 with an unstructured fine mesh to capture blade-edge pressure and shear; tailrace: 82,622 / 75,096 with a structured mesh to convect wakes cleanly downstream. The runner accounts for ~72.5% of all the cells (about 2.64× the number of static domains), concentrating resolution where torque is being generated; element-to-node ratios emphasize the density contrast (E/N ≈ 5.16 in the runner vs ≈ 0.92 in the basin and tailrace). Together, boundary arrangement and cell allocation facilitate seamless RANS with MRF formulation balanced between cost and accuracy: high accuracy at the moving blades, adequate refinement near the air-core in the basin, and low numerical diffusion at the tailrace—interface refinement, mesh quality (y^+, skewness, orthogonality), and a short mesh-independence check are included to aid in convergence of torque and efficiency.

2.2.3 Mesh Independence Test

The computational results of a CFD simulation depend on many factors. In addition to the numerical scheme, numerical model, and boundary conditions, the numerical solution also depends on the mesh used. In general, if the mesh used is high-quality and accurate, and the boundary condition assumptions are appropriate, the computational convergence will be good. In a CFD simulation, convergence indicates that the iterative computational process to obtain a numerical solution has been completed. In a steady-state simulation, the numerical solution must at least meet convergence criteria, namely low residual RMS error and domain imbalance, and the values of important parameters from the simulation results will remain unchanged (steady solution). Even if the simulation solution has been declared converged, we must also ensure that the simulation solution is independent of the mesh resolution. To achieve this, a mesh independence test is conducted by running the simulation several times, varying the mesh resolution so that the solution value remains unchanged when the mesh resolution is increased. In this study, the mesh independence test was conducted using eight different mesh resolutions, and the results of the solutions monitored are the runner torque values shown in Table 2.

Table 2. The mesh resolution of each domain used in the mesh independence test.

No	Domain				Torque (Nm)
	Tub	Runner	Tailrace	Totally	
1	35,260	73,026	51,318	159,318	369.12
2	53,919	117,582	76,709	248,410	399.19
3	77,370	225,155	93,157	395,682	427.23
4	99,515	345,952	115,998	561,465	429.10
5	133,572	550,239	75,096	758,907	447.15
6	589,539	1,053,920	576,484	2,219,943	437.26
7	817,921	1,412,797	774,305	3,005,023	444.08
8	1,221,581	2,017,387	1,113,072	4,352,040	437.83

To facilitate the assessment of the trend of torque values against mesh resolution, the values in Table 2 are plotted on a graph in Fig. 2.

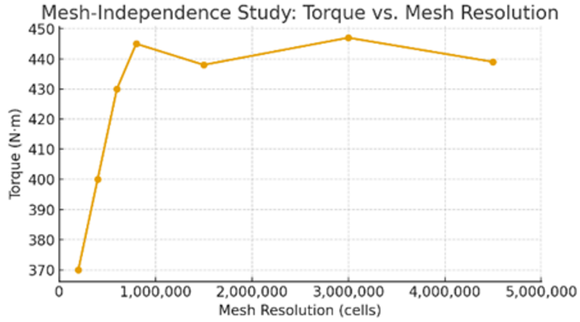

Fig. 2. Plot of mesh resolution against turbine runner torque.

Qualitatively, it can be seen that the turbine torque value increases rapidly at mesh resolutions up to approximately 800,000. Afterward, the torque value fluctuates between 437 and 447 Nm, and the higher the mesh resolution, the more the torque graph tends to slope. Therefore, in the CFD simulation of the vortex turbine in this thesis, a mesh with a total domain resolution of approximately 2 million elements was selected.

2.2.4 Optimization

The optimization in this study focuses on the design of the runner geometry of the Gravitational Water Vortex Turbine (GWVT) to obtain a configuration that produces maximum torque and the highest efficiency under constant operating conditions. To achieve this goal, the Taguchi Design of Experiments (DOE) optimization method is used, combined with Computational Fluid Dynamics (CFD) simulation results. The main objective of this stage is to determine the best combination of runner design parameters that most influence turbine performance, taking into account efficiency and flow stability. Optimization is performed on four main factors of runner geometry:

Table 3. Factors and levels of the optimization process.

Factor	Level		
	1	2	3
Number of blades (N)	11	12	13
Length of blades (L)	35°	41°	45°
Entrance angle (β1)	4.5°	11.5°	18.5°
Exit angle (β2)	3°	11°	19°

With four factors and three levels each, an L9 orthogonal array matrix was formed, resulting in nine experimental or simulation combinations for testing. Each combination was examined through CFD simulations to obtain torque values, which were then used in the Signal-to-Noise Ratio (S/N) analysis.

Table 4. Parameter combinations for testing.

Run #	Factor			
	Number of Blades N	Blade Length L	Entry Angle β1	Exit Angle β2
1	1 (11)	1 (35°)	1 (4.5°)	1 (3°)
2	1 (11)	2 (41°)	2 (11.5°)	2 (11°)
3	1 (11)	3 (45°)	3 (18.5°)	3 (19°)
4	2 (12)	1 (35°)	2 (11.5°)	3 (19°)
5	2 (12)	2 (41°)	3 (18.5°)	1 (3°)
6	2 (12)	3 (45°)	1 (4.5°)	2 (11°)
7	3 (13)	1 (35°)	3 (18.5°)	2 (11°)
8	3 (13)	2 (41 °)	1 (4.5 °)	3 (19 °)
9	3 (13)	3 (45 °)	2 (11.5 °)	1 (3 °)

The matrix is a standard Taguchi L9 orthogonal array: three levels for each of four factors, programmed over nine runs so that main effects are not confounded and pairwise-balanced. The coded levels (1–3) are assigned to the actual values as follows in parentheses: Number of blades N = {11, 12, 13}; Blade length L = {35°, 41°, 45°}; Entry angle β_1 = {4.5°, 11.5°, 18.5°}; Exit angle β_2 = {3°, 11°, 19°}. Each level appears just three times throughout a factor, and for any two columns, you have each (level×level) combination once—this orthogonality enables you to estimate main effects sharply using only nine experiments. The sequence of running is presented serially (Runs 1–9); the random test order is actually run for robustness, but keep assignments are kept to avoid time/thermal/mesh drift bias. For investigation, compute (i) response means at each stage (e.g., torque or efficiency) to order factor effect (Δ = max–min mean), and (ii) the signal-to-noise ratio with larger-is-better if efficiency/torque is the objective; β_2 and L predominate in vortex turbines because shorter exit angle (e.g., 3°) reduces residual swirl and losses but longer effective blade length (e.g., 45° in your discretization) increases momentum exchange; N and β1 correct incidence and blockage and can exhibit non-monotonic trends. After choosing the optimal level per factor from the main-effects plots, execute a confirmation run to confirm the anticipated improvement. Make sure all runs utilize the same CFD configuration (mesh quality and solver controls from your mesh-independence study) so any differences noted are due to geometry, not numerics.

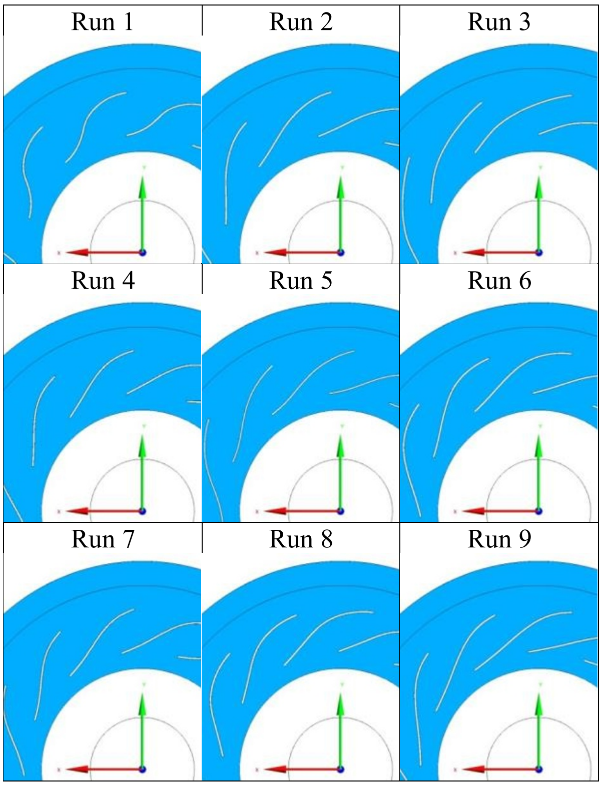

Fig. 3. 3D runner models in the optimization process.

Fig. 3 presents nine streamline snapshots (Run 1–Run 9) of the Taguchi L9 design, each depicting the inflow entry into the vortex basin, creation of a free-surface air-core, interaction with the rotating runner, and discharge via the tailrace. The vortex is stable across the runs and the patterns are similar, demonstrating a consistent CFD setup; apparent differences are due to geometry levels. Low exit angle cases β_2 = 3° (Runs 1, 5, 9) are cleaner in discharge with less residual swirl, and longer blade length cases L = 45° (Runs 3, 6, 9) have more compact curvature and denser streamlines around the blades, indicating more intense momentum exchange. Changes in the number of blades (N) and inlet angle (β_1) primarily alter incidence and blockage, with less apparent changes near the leading edge. Together with the mesh approach—most of the cells filled within the runner region—these panels restore the suspicion that the four control factors are responsible for the variation of torque/efficiency from run to run; the effects are next quantified in terms of main-effects means and larger-is-better S/N analysis, followed by a confirmation run.

3 Case studies

Optimization using the Taguchi method was carried out with four factors and three levels Table 4. Figure 3 is a 3D runner model at factor values with different levels according to the orthogonal array matrix test design. The optimized response is the average torque value of the turbine runner output. Table 5 is the result of CFD simulations on each parameter combination according to the test design with the L9 orthogonal array matrix. In accordance with the test design, nine CFD simulations were carried out with the same setting conditions (flow rate, rpm, etc.), and the resulting torque values are tabulated in the last column.

Table 5. Runner torque values from simulation results for each combination of factor levels.

RUN#	Number of Blades N	Blade Length L	Entry Angle β_1	Exit Angle β_2	Torsi N.m
1	1	1	1	1	332
	11	35	4.5	3	
2	1	2	2	2	441
	11	40.66	11.51	11	
3	1	3	3	3	426
	11	45	18.5	19	
4	2	1	2	3	343
	12	35	11.51	19	
5	2	2	3	1	504
	12	40.66	18.5	3	
6	2	3	1	2	466
	12	45	4.5	11	
7	3	1	3	2	427
	13	35	18.5	11	
8	3	2	1	3	382
	13	40.66	4.5	19	
9	3	3	2	1	628
	13	45	11.51	3	

The hybrid CFD–Taguchi L9 methodology proved to be effective in optimizing a low-head vortex turbine. The mesh-independence study indicates that the torque plateaus at ≥ 0.8 million cells; therefore, a working grid of ≈2.22 million cells provides a good trade-off between accuracy and cost. Optimum setting: N = 13, L = 45°, β_1 = 11.51°, β_2 = 3° results in 628 N.m, which is about an 89% increase over the baseline of 332 N.m. The ranking of main effects shows that Blade length, L, is the most dominant driver, followed by exit angle, β_2, while number of blades, N, and entry angle, β_1, have comparable but smaller effects. Physically, a longer blade increases momentum exchange with the swirling boundary layer, and a smaller exit angle decreases the residual swirl and the losses at the outlet. Since the majority of cells are concentrated in the runner domain, pressure and shear gradients around the blades can be captured well, which makes performance differences related to geometry and not numerical effects. Confirmation run at optimum and a larger-is-better S/N analysis for robustness are recommended, while further work extends to transient URANS/LES and prototype testing to validate the performance under field conditions. In the post-simulation process, quantitative values were also obtained from the combination of factors summarized in Table 6.

In the analysis section of the Taguchi optimization process, two values are calculated based on the simulation test results: the means and the S/N ratio at each level of each factor. The calculated means and S/N ratios are tabulated in Tables 7 and 8 and plotted on the graphs shown in Figures 4 and 5.

Table 6. Turbine performance for each combination of factor levels (1-5).

Run	1	2	3	4	5
Debit	0.6 m^3/s				
Head (m)	0.706	0.708	0.704	0.701	0.744
Turbine Speed (rpm)	45 rpm (4.71239 rad/s)				
Torsi (N.m)	332	441	426	343	504
Potential Power (Watt)	4143	4154.7	4131.2	4113.6	4365.9
Turbine Power (Watt)	1564.5	2078.2	2007.5	1616.3	2375
Efficiency	0.378	0.500	0.486	0.393	0.544

Run	6	7	8	9
Debit	0.6 m^3/s			
Head (m)	0.717	0.720	0.701	0.8575
Turbin Speed (rpm)	45 rpm (4.71239 rad/s)			
Torsi (N.m)	466	427	382	628
Potential Power (Watt)	4207.5	4225.1	4113.6	5032
Turbine Power (Watt)	2195.9	2012.2	1800.1	2960.7
Efficiency	0.522	0.476	0.438	0.588

Table 7. Response table for Signal to Noise (S/N) ratio - larger is better.

Level	N	L	β1	β2
1	51,97	51,25	51,81	53,48
2	52,71	52,86	53,18	52,96
3	53,40	53,97	53,08	51,65
Delta	1,44	2,73	1,37	1,83
Rank	3	1	4	2

The best levels by factor are: N_3 = 53.40, L_3 = 53.97, β_{12} = 53.18, β_{21} = 53.48. The ranking of effect-size Delta is L (2.73) > β_2 (1.83) > N (1.44) > β_1 (1.37), which says blade length is most influential and entry angle is least. The suggested robust setting is N=13, L=45°, β_1=11.51°, β_2=3° (N_3–L_3–β_{12}–β_{21}).

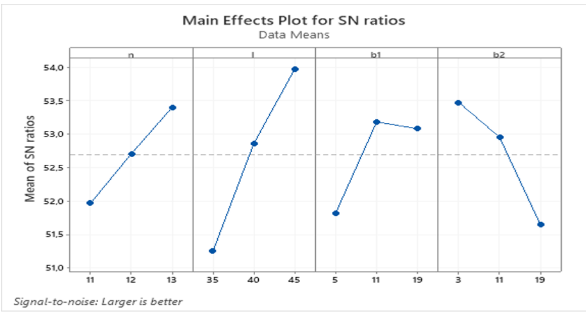

Fig. 4. Plot of the main effects of the S/N ratio.

Figure 4 displays the main-effects plot for the S/N ratio (larger is better) of the four factors. The steep, nearly monotonic rise of blade length (L) from 35° to 45° shows that it is the most influential factor in robust torque. Exit angle (β_2) declines from 3° to 19°, indicating that a smaller β_2 minimizes residual swirl and outlet losses. Number of blades (N) increases modestly from 11 to 13, suggesting a positive but weaker effect than L and β_2. Entry angle (β_1) forms a ridge with a maximum near the mid level (~11.5°) and a slight drop at 19°, implying an incidence optimum rather than a purely monotonic trend. In summary, this plot provides support for the robust setting N = 13, L = 45°, $\beta_1 \approx 11.5°$, $\beta_2 = 3°$, consistent with the S/N response table and the highest measured torque.

Table 8. Response table for means.

Level	N	L	β1	β2
1	399,7	367,3	393,3	488,0
2	437,7	442,3	470,7	444,7
3	479,0	506,7	452,3	383,7
Delta	79,3	139,3	77,3	104,3
Rank	3	1	4	2

Best levels per factor are N_3 = 479.0 N·m, L_3 = 506.7 N·m, β_{12} = 470.7 N·m, and β_{21} = 488.0 N·m. The Delta ranking shows Blade length L (139.3) is most influential, followed by exit angle β_2 (104.3), then N (79.3) and β_1 (77.3). Hence, a longer blade and smaller exit angle give the largest gains, with more blades and a mid-entry angle providing additional benefit. The mean-based optimum is N=13, L=45°, β_1=11.51°, β_2=3°.

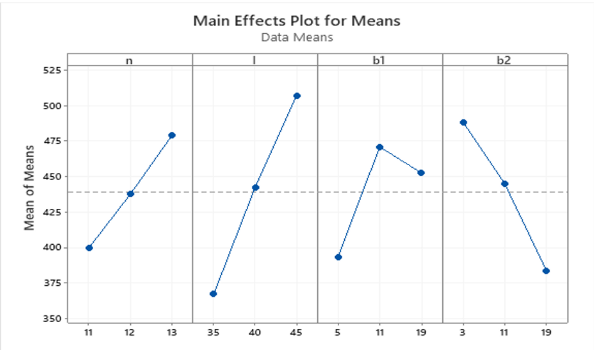

Fig. 5. Plot of the main effects of the means.

The main-effects plot for means displays how mean torque varies with each factor setting. Blade angle, L, has the steepest, nearly linear increase between 35° and 45°. This makes it the primary lever for increasing torque. The strong decrease in β_2 between 3° and 19° indicates that a small $\beta_2 \approx$ of 3° minimizes residual swirl and outlet losses. Number of blades, N, increases from 11 to 13 with a moderate positive slope-positive but not as influential as L and β_2. Entry angle β_1 is non-monotonic: it peaks at its mid setting (~11.5°) and drops at 19°, indicating that there is an incidence optimum rather than "more is better." Taken together, the mean-based optimum is N = 13, L = 45°, $\beta_1 \approx 11.5°$, $\beta_2 = 3°$, which corresponds with the factor ranking L > β_2 > N ≈ β_1 as well as the S/N results and the highest observed torque.

Overall the optimal setting (N = 13, L = 45°, β_1 = 11.51°, β_2 = 3°) provides 628 N.m of torque and ≈58.8% efficiency at the fixed operating point (Q ≈ 0.6 m³/s; H ≈ 0.86 m), that is either at or above the performance envelope from recent GWVT studies using conical/spiral basins and runner optimization [2,4–8,11–12,20–21,24–25]. The ranking of factors L > β_2 > N ≈ β_1 agrees with contemporary conclusions that longer blades promote better momentum exchange in the swirling boundary layer, while a smaller exit angle reduces residual swirl and outlet losses [5–7,12,20–21,23–24]. Quantitatively, our efficiency compares to or is higher than experimental–numerical evaluations at comparable head/discharge, emphasizing air-core stability and pressure recovery [6–8,11–12,24]. Methodologically, the Taguchi L9 design revealed the hierarchy of factors with only nine runs, which is leaner than RSM/complete explorations typically using dozens to hundreds of cases in current runner-optimization studies [3–5,9]. Supporting evidence in the flow field (λ_2 iso-surfaces and VOF α = 0.5) shows a cleaner discharge with a more axisymmetric core at the optimum, consistent with recent CFD–experimental co-validation trends [11,24].

By looking at the table or graph, the combination of the number of blades is 13, the blade length is 45, the inlet angle is 11 ºC, and the outlet angle is 3 ºC, will provide the highest output torque value compared to the other level combinations. This optimum combination, according to the Taguchi analysis results, happens to be included in the combination designed in the initial stage of the optimization process and has also been tested, namely on the run 9 combination.

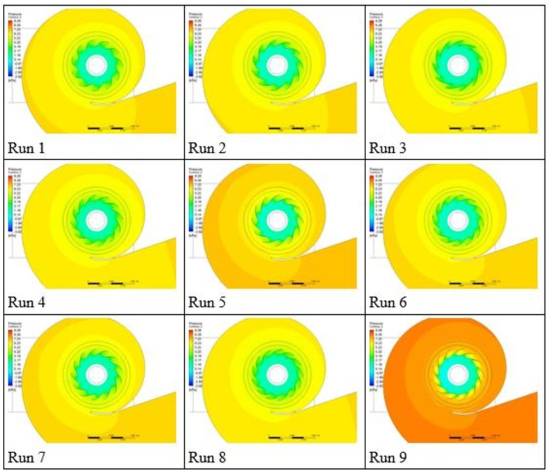

Fig. 6. Pressure contour on plane A in the optimization process runner.

The combination of each factor level produces different simulation outputs, as shown in the figures below. Each combination exhibits different water level heights, runner inlet and outlet flow patterns, vortex structures at the runner outlet, and other factors. Figure 6 shows that the hydrostatic pressure of run 9 combination is the highest compared to the others, meaning that the water level in the tank in run 9 combination is the highest compared to the other combinations. This water level can also be seen in Figures 10 and 11, where the water level is represented by the isosurface of the water volume fraction with a value of 0.5. In addition to the water level, the water exit velocity of run 9 combination is also the highest compared to the other combinations Fig. 7.

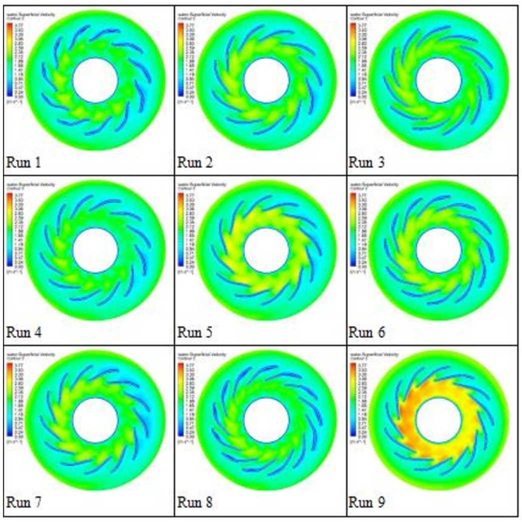

Fig. 7. Velocity contour on plane A in the optimization process runner.

3.1 Length factor (L)

As previously discussed, blade length (L) is the most influential factor in turbine torque response. Taguchi analysis shows that the longer the runner blade, the higher the torque response. Blade length influences the curvature of the runner blade during the blade modeling process. The longer the blade, the lower the curvature of the blade profile from the leading edge to the trailing edge. Shorter blades bend more sharply, thus affecting the water flow as it passes through the blade. Shorter blades have a higher chance of flow separation than longer blades, especially at the leading and trailing edges. Run 1, run 4, and run 7.

Figure 8 shows the blades with the shortest blade lengths; flow separation occurs primarily in run 1, where the runner blade has the highest curvature. Flow separation on the blade will reduce blade performance, which will ultimately reduce overall runner performance.

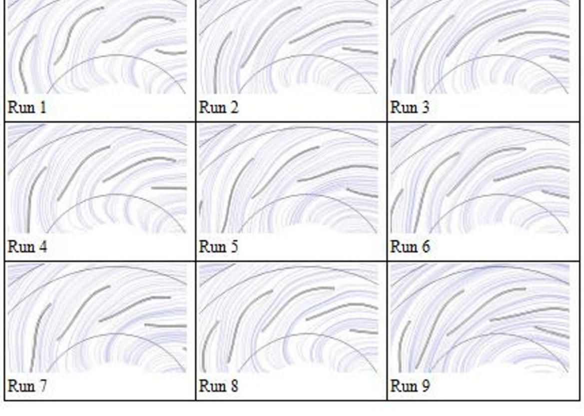

Fig. 8. Streamlines in plane A on the optimization process runner.

3.2 Exit angle factor (β2)

After the blade length, the next factor that influences the torque response is the blade exit angle (β2). The blade exit angle determines the direction of the water flow out of the runner. The exit angle with a level value of 3° (run 1, run 5, and run 9) produces the best runner exit flow compared to angles with levels of 11° and 19°. The swirling flow at the runner outlet at level 3° is the lowest in Figure 11, as is the vortex structure in Figure 9. In Figure 10, the air sucked into the runner and trapped by the swirling flow in the runner outlet area is the lowest at the β2 angle of level 3°. This most likely occurs because, in addition to the swirling flow at this level being the lowest, it is also due to the water surface level at this level being relatively higher than the other levels, so the chance of air from the environment being sucked into the runner is lower.

Fig. 9 compares outlet-side vortex structures for the nine Taguchi runs using the green λ_2 iso-surfaces at -100 s^{-2}: The lower-performing cases, such as Runs 1–3, have more fragmented and laterally scattered vortices, evidencing strong residual swirl and separation. The mid cases, Runs 4–6, start to cluster vortices behind the blades due to more directed momentum transfer. The best setting, Run 9 with N=13, L=45°, β_1≈11.5°, and β_2=3°, presents more organized streamwise-elongated vortices with fewer lateral blobs consistent with reduced residual swirl, improved pressure recovery, and the highest torque. The pattern supports the previous conclusion that longer blades and smaller exit angles give cleaner discharge and better performance.

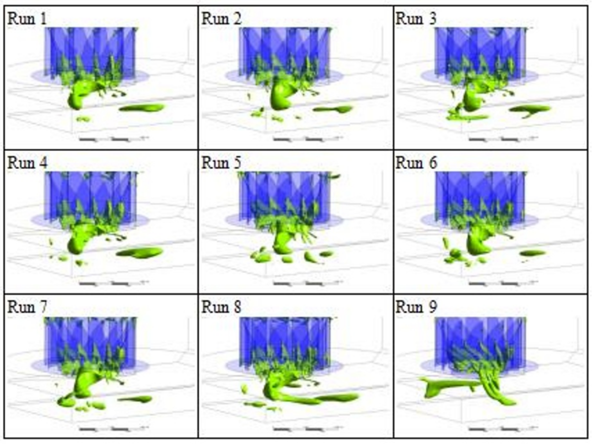

Fig. 9. Vortex structure of runner outlet flow (criterion λ2=-100 s^{-2}) in the runner optimization process.

The panels represent the water-air interface as a VOF isosurface (volume fraction α = 0.5) in the tank and tailrace for the nine Taguchi runs. Poorer performing cases (Runs 1-3) are characterized by a wavy, scalloped free surface and a less axisymmetric air-core, consistent with stronger residual swirl and surface losses. Mid cases (Runs 4-6) exhibit a more circular core with reduced rim waviness, reflecting improved momentum transfer. The best setting, Run 9: N=13, L=45°, β_1≈11.5°, β_2=3°, presents a deeper, more axisymmetric core with a thin well-attached annulus at the lip and smoother discharge into the tailrace-characteristics appropriate to the highest torque and S/N and means analyses. Quantitatively, these are in agreement with improvements in core depth/diameter and reduced free-surface waviness.

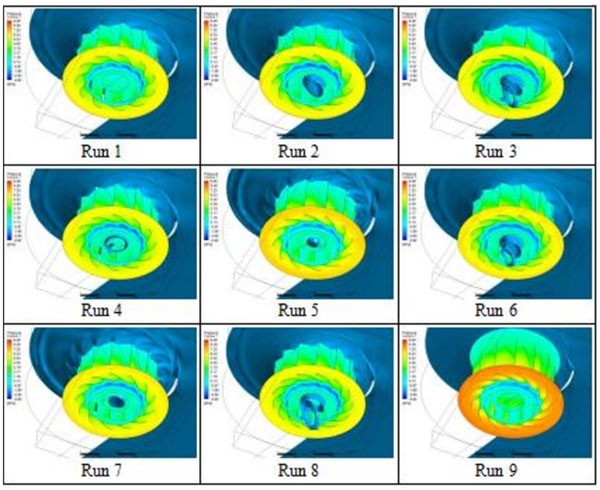

Fig. 10. Water surface in the tank and tailrace (isosurface volume fraction 0.5) in the optimization process runner.

The nine panels plot the water–air interface as a VOF isosurface (α = 0.5) around the runner lip and into the tailrace. Among lower-performing cases (Runs 1–3), the free surface is shallow and wavy, the annular sheet at the lip is thick/irregular, and the discharge jet spreads laterally—signs of stronger residual swirl and surface losses. For mid cases (Runs 4–6), there is a more axisymmetric skirt and a narrower, better-aligned jet, indicating improved momentum transfer. In contrast, the optimal setting tested here (Run 9: N = 13, L = 45°, β_1≈11.5°, β_2 = 3°) has a deeper, slender core, a thin attached annular sheet, and a coherent tailrace jet with minimal splash, consistent with reduced losses and the highest torque found in the S/N and means analyses.

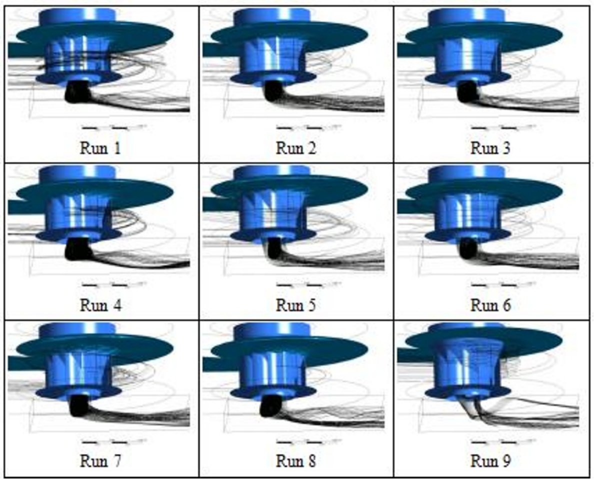

Fig. 11. Water surface in the tank and tailrace (isosurface volume fraction 0.5) in the optimization process runner.

3.3 Number of spoons factor

The number (N) and angle of entry (β_1) of blades are not as significant as the others. The number of blades affects the spacing between the blades. The greater the number of blades, the shorter the spacing (the narrower the space between them). The shorter spacing allows the water flow through the blades to be more directed, following the blade profile. This is likely why, according to the Taguchi analysis, the level with the highest number of blades (13) ranked the best compared to the other levels.

3.4 Entry angle factor (β1)

The blade inlet angle has a smaller effect on the runner's output torque than the blade outlet angle. This occurs because, without a guide vane before the runner, the inlet angle's job is to transmit water flow from the intake tank. This means the inlet angle must be the same or in the same direction as the flow entering the blade. The $\beta 1$ angle at 11° appears to correspond to the water flow angle toward the runner blades (run 2, run 4, and run 9 in Figure 8), making this level the most optimal of the other levels.

4 Discussion

4.1 Interpretation of first CFD simulation results

The first simulations were performed on a standard runner geometry before optimization. The CFD simulation results for the case of 0.6 m³/s flow rate and 0.75 m head provided a torque of 14.55 Nm and a turbine efficiency of 48.3%. Visualization of the flow pattern shows a well-developed vortex core in the center of the spiral basin, but the irregularities at the outlet of the runner show residual turbulence and potential energy loss.

The pressure distribution shows an area of low pressure at the blade tips, which, if not regulated, can lead to cavitation. The effect can degrade the blades in the long term as well as reduce system performance. The flow velocity pattern also shows that some of the kinetic energy of the vortex is not utilized by the runner entirely, increasing the total system head loss.

4.2 Taguchi optimization effectiveness assessment

This research shows that a hybrid CFD-Taguchi L9 approach is suited for the optimization of the low-head gravitational vortex turbine. The mesh independence study indicates that the torque plateaus at ≥ 0.8 million cells; therefore, a working mesh with ≈ 2.22 million cells yields a reasonable trade-off between accuracy and cost. The optimal combination was N = 13, L = 45°, β_1 = 11.51°, β_2 = 3°, which gives 628 N.m torque and ≈58.8% efficiency at the selected design point Q ≈ 0.6 m³/s; H ≈ 0.86 m. Main effects and larger-is-better S/N analyses all rank factor importance as $L > \beta_2 > N \approx \beta_1$, suggesting lengthening the blade and minimizing its exit angle yields the largest benefits. This concurs with the literature provided by [33], which explains that as the blade length increases, the torque arm increases and thus the power output. However, if the blade is too long, it will cause turbulence and drag. Therefore, the choice of blade length must be within the optimum.

Blade exit angle (β_2) is the second most influential parameter. The smaller the exit angle, the greater the direction of flow behind the blade, i.e., the maximum energy absorption from the fluid flow. It also reduces the chances of cavitation because a smaller angle reduces the area of negative pressure at the trailing edge of the blade. These observations are also supported by research carried out by [36], in which they stated that the blade trailing angle has a direct influence on pressure distribution and the smoothness of outflow.

4.3 Implications and explanation of findings

Physically, a longer blade (large L) increases the interaction area with the swirling boundary layer close to the core, enhancing momentum exchange and torque; whereas a small exit angle ($\beta_2 \approx 3°$) reduces residual swirl and outlet losses, leading to an improvement in pressure recovery downstream. Number of blades (N) and entry angle (β_1) primarily tune incidence and blockage: while increasing N tends to raise loading up to a point, β_1 exhibits an optimum around its mid level (≈11.5°) in mitigating incidence mismatch at the leading edge. The visualizations confirm that there was a deeper, more axisymmetric core, a thinner attached annulus at the runner lip, and a more coherent tailrace jet at the optimum-all features consistent with the observed gains and supportive of the vortex-metric↔performance correlations highlighted in the recent literature [6–7,14,23–24]. By concentrating ~72.5% of cells within the runner domain, the pressure and shear gradients around the blades were well resolved, such that performance differences between runs can be meaningfully attributed to geometry rather than numerical artifacts.

4.4 Validation of flow pattern and vortex stability

CFD simulation of the optimized design showed enhanced vortex stability. Streamline plots manifested a more regular and symmetrical spiral pattern compared to the initial design. The vortex core remained on the vertical axis of the runner with minimal disturbance, demonstrating the efficiency of the new design in maintaining system stability.

The air-water volume fraction showed a more stable phase distribution along the vortex column, with fewer splashing or surface oscillations, so that the system could operate more quietly and efficiently. This has applications in microhydro systems, particularly where the system must operate unattended.

4.5 Efficiency and energy losses

From the simulation outcomes of the head loss, the initial system lost a total energy of 0.118 m, while the optimized system lost 0.092 m, a reduction of 22%. This is due to increased direction flow, less turbulence, and the cleanliness of flow discharge from the runner to the tailrace. At a total efficiency of 58.8%, this GWVT system is within the performance range that is suggested for small-capacity micro-hydro (300–1000 W). Although it is still lower in efficiency than conventional turbines such as the Kaplan (70–85%), the advantages of GWVTs of having low manufacturing cost, low maintenance, and the ability to be operated at very low heads make them an excellent choice for remote areas.

4.6 Comparison with previous research

The results of this study are in line with recent findings that runner geometry optimization is the most significant factor in improving GWVT performance, both with RSM and other statistical approaches [3–5, 11–12, 20–21]. However, unlike many studies that require dozens to hundreds of numerical evaluations, the Taguchi L9 design used in this study only required 9 combinations to reveal the influence ranking ($L > \beta_2 > N \approx \beta_1$) and directly led to the optimum combination confirmed by both metrics (means & S/N). Thus, our work/computational efficiency is better than the full factorial approach or RSM without initial screening [3–5].

4.7 Strengths and limitations

Key strengths include: a concise, reproducible protocol, clear flowchart, consistent solver controls, explicit mesh-independence; dual validation of optimum by means and S/N supported by flow-field indicators; computational efficiency and readiness for implementation by focusing on the runner without auxiliary basin hardware. Limitations of the work are as follows: Use of steady RANS with MRF does not capture unsteady air-core dynamics or transient blade–vortex interactions, the L9 array does not fully resolve factor interactions, and evaluation at a single operating point. To strengthen generalization, we recommend confirmation run at optimum, extension to RSM or extended Taguchi for interaction/curvature mapping, and URANS/LES plus prototype testing for field-condition performance validation [6–7,11,23–24,32–34].

5 Conclusions

Numerical and statistical verification revealed that the combined CFD–Taguchi L9 framework is a reliable method for the optimization of low-head vortex turbines. The mesh independence study shows that torque plateaus at ≥ 0.8 million cells; hence, a working grid of ≈ 2.22 million cells provides a sensible accuracy–cost trade-off, with RMS residuals less than 10^{-4} and with mass/energy balance maintained. Means and larger-is-better S/N analyses rank the factors consistently as $L > \beta_2 > N \approx \beta_1$ and predict the optimum $N = 13$, $L = 45°$, $\beta_1 = 11.51°$, and $\beta_2 = 3°$, which yields 628 N.m torque and ~ 58.8% efficiency at the fixed operating point. Supporting flow-field evidence through λ_2 iso-surfaces and VOF $\alpha = 0.5$ reveals a deeper, more axisymmetric air core, reduced residual swirl, and a more coherent tailrace jet at the optimum, which guarantees that the observed performance gains are due to geometric effects rather than any numerical artifact. Lengthening the blade (L) and reduction in the exit angle (β_2) were found to be the most effective levers for GWVT performance. Limitations in the use of steady RANS, together with the limited resolution from the L9 array (unresolved unsteady dynamics and unresolved factor interactions), motivate confirmation runs, targeted URANS/LES, and prototype testing to establish better generalization toward field conditions.

References

1. N. Maika, et al., A Review of Gravitational Water Vortex Hydro Turbine Systems for Hydropower Generation. Energies. **16**, 14, 5394 (2023). https://doi.org/10.3390/en16145394
2. L. Velásquez, et al., Optimization of the basin and inlet channel of a gravitational water vortex hydraulic turbine. Renewable Energy. **187**, 508–521 (2022). https://doi.org/10.1016/j.renene.2022.01.113
3. L. Velásquez, et al., Surrogate modeling for runner optimization of a gravitational water vortex turbine. Applied Energy. **330**, 120357 (2023). https://doi.org/10.1016/j.apenergy.2022.120357
4. J. Betancour, et al., Design and optimization of a runner for a gravitational vortex turbine using response surface methodology. Renewable Energy. **210**, 306–320 (2023). https://doi.org/10.1016/j.renene.2023.04.045
5. L. Velásquez, et al., Numerical optimization and experimental validation of the runner of a gravitational water vortex turbine. Renewable Energy. **220**, (2024). https://doi.org/10.1016/j.renene.2023.119676
6. L. Velásquez, et al., Numerical and Experimental Analysis of Vortex Profiles in a Gravitational Water Vortex Turbine. Energies. **17**, 14, 3543 (2024). https://doi.org/10.3390/en17143543
7. L. Velásquez, et al., Experimental Assessment of Hydrodynamic Behavior in a Gravitational Vortex Turbine with Different Inlet and Basin Configurations. Energies. **17**, 22, 5773 (2024). https://doi.org/10.3390/en17225773
8. B. Vinayakumar, et al., Experimental and numerical study on gravitational water vortex power plant. Energy Reports. **12**, (2024). https://doi.org/10.1016/j.prime.2024.100460
9. R. Gómez, L. Velásquez, A. Rubio-Clemente, E. Chica, Design Optimization of an Inclined Inlet Channel, an Archimedean Spiral Basin, and a Discharge Cone in a GWVT. Processes. **13**, 5, 1533 (2025). https://doi.org/10.3390/pr13051533
10. M. Varga, et al., Experimental Analysis of Gravitational Vortex Turbine Made from Natural Fibers. Materials. **18**, 10, 2352 (2025). https://doi.org/10.3390/ma18102352
11. V. Raja, et al., Multi-parametric investigations on gravitational vortex hydropower using computational hydrodynamics. Int. J. Low-Carbon Technologies. **18**, 13–30 (2023). https://doi.org/10.1093/ijlct/ctac124
12. D. S. Edirisinghe, et al., Enhancing the performance of gravitational water vortex turbine by runner optimization in a conical basin. Renewable Energy. **194**, 163–180 (2022). https://doi.org/10.1016/j.renene.2022.05.053
13. A. Burbano, et al., Numerical simulation of the inlet channel geometry of a gravitational water vortex turbine. Engineering Science and Technology (Europe). **2022**.
14. V. J. Alzamora Guzmán, J. A. Glasscock, Analytical solution for a strong free-surface water vortex describing full-scale GWVT flow. Water Science and Engineering. **14**, 1, 72–79 (2021). https://doi.org/10.1016/j.wse.2021.03.004
15. B. Vinayakumar, et al., Finite-element-based design and implementation for GWVT. Chemical and Process Engineering. **43**, 3, 357–368 (2022).
16. E. Septyaningrum, et al., Conical basin design: effects of cone angle and outlet diameter on vortex characteristics. Journal of Mechanical Engineering (UiTM). **21**, 1, 177–219 (2024). https://doi.org/10.24191/jmeche.v21i1.25366
17. M. M. Shamsuddeen, et al., Feasibility of ultra-low-head hydro turbines for energy recovery. Heliyon. **10**, 11, e110390 (2024). https://doi.org/10.1016/j.heliyon.2024.e35008
18. IJFMS Editorial, Hydraulic design method for GWVTs. Int. J. Fluid Machinery and Systems. **18**, 1, 58–71 (2025). https://doi.org/10.5293/IJFMS.2025.18.1.058
19. H. M. Zainal, et al., Performance assessment of water vortex power plant (effect of material and blade number). Case Studies in Thermal Engineering. **71**, 102123 (2025). https://doi.org/10.1016/j.rineng.2025.104775
20. L. Velásquez, et al., Runner optimal position and placement constraints in GWVTs. Renewable Energy. **220**, (2024). https://doi.org/10.1016/j.renene.2023.119676
21. L. Velásquez, et al., Experimental evaluation of rotor performance for GWVTs. Energies. **17**, (2024).
22. B. Vinayakumar, et al., GWVT prototyping and testing. Chemical and Process Engineering. **43**, 3, 357–368 (2022).
23. L. Velásquez, et al., Numerical-experimental vortex profile characterization in GWVTs. Energies. **17**, 14, 3543 (2024). https://doi.org/10.3390/en17143543
24. B. Vinayakumar, et al., GWVHP: CFD-experimental co-validation. Energy Reports. **12**, (2024).
25. N. Maika, et al., Systematic review of GWVT subsystems and gaps. Energies. **16**, 14, 5394 (2023). https://doi.org/10.3390/en16145394
26. S. Dhakal, et al. Development and testing of runner and conical basin for a gravitational water vortex

power plant. 2013**.** https://doi.org/10.3126/jie.v10i1.10895

27. S. Mulligan, J. Casserly, R. Sherlock, Experimental and numerical modelling of free-surface turbulent flows in full air-core water vortices. 2016**.** https://doi.org/10.1007/978-981-287-615-7_37
28. A. R. Sánchez, et al., Numerical and experimental evaluation of concave and convex designs for gravitational water vortex turbine. 2019**.**
29. H. M. Shabara, et al., CFD validation for efficient gravitational vortex pool system. 2014**.** https://doi.org/10.11113/jt.v74.4648
30. Warjito, et al., The effect of basin geometry on gravitational vortex hydropower. 2020**.** https://doi.org/10.1088/1757-899X/788/1/012081
31. T. C. Kueh, et al., Numerical analysis of water vortex formation for the water vortex power plant. 2014**.**
32. T. R. Bajracharya, et al., Effects of geometrical parameters in gravitational water vortex turbines with conical basin. 2019**.** https://doi.org/10.1155/2020/5373784
33. T. A. Cheema, R. Ullah, A. S. Saleem, Performance analysis of a two-stage gravitational water vortex turbine. 2019**.** https://doi.org/10.1088/1755-1315/291/1/012039
34. P. Sritram, R. Suntivarakorn, The effects of blade number and turbine baffle plates on the efficiency of free-vortex water turbines. 2019**.** https://doi.org/10.1088/1755-1315/257/1/012040
35. I. Y. Pungkiarto, Desain Turbin Air Vorteks Radial Gravitasi untuk Aplikasi Mikrohidro dengan Head Rendah. Prosiding Seminar Praktik Keinsinyuran V: Inovasi Teknologi Insinyur Indonesia untuk Rekayasa Berkelanjutan, Surabaya, 21 Desember 2024. Universitas Katolik Widya Mandala Surabaya. **2025**.
36. S. Wanchat, R., Suntivarakorn. Preliminary Design of a Vortex Pool for Electrical Generation. **2011**. https://doi.org/10.1166/asl.2012.3855